International Forum on Aeroelasticity and Structural Dynamics
IFASD 2017
25-28 June 2017 Como, Italy

WIND-TUNNEL TESTING FOR VALIDATION OF A METHOD FOR NONLINEAR FLUID/STRUCTURE INTERACTION USING SURROGATE MODELS.

Elisa Bosco[1], Albert Lucchetti[1], Simon Trapier[1], F. G. Di Vincenzo[2], N. Gourdain[3], J. Morlier[4]

[1]Airbus Operations SAS
316 Route de Bayonne - 31300 Toulouse France
elisa.bosco@airbus.com
albert.lucchetti@airbus.com
simon.trapier@airbus.com

[2]MSC.Software
4, Rue du Professeur Pierre Vellas - Europarc, Immeuble Jupiter, B10 - 31300 Toulouse, France
FaustoGill.DiVincenzo@mscsoftware.com

[3]Université de Toulouse, ISAE
DAEP, 10 Avenue Edouard Belin, 31055 Toulouse Cedex 4, France
Nicolas.GOURDAIN@isae.fr

[4]Université de Toulouse, Institut Clément Ader, ISAE
10 Avenue Edouard Belin, 31055 Toulouse Cedex 4, France
Joseph.MORLIER@isae.fr

Keywords: Fluid Structure Interaction, Nonlinear transient response, Wind tunnel testing, Validation

Abstract: This article describes the data collection techniques and interprets the acquired data for validating a method for simulating fluid structure interaction. The method combines structural and aerodynamic reduced order models, interpolation techniques, and an efficient aero-structure data exchange to estimate non-linear fluid structure interaction during transient response in order to reduce the simulation time. Data are collected through wind tunnel testing and validation is done through direct comparison between simulation and test-data.

1 INTRODUCTION

A fluid-structure interaction problem requires the solution of the coupled equations of both the fluid and the structure. This can be computationally highly intensive and extremely time-costly depending on the complexity of the phenomena to be predicted. Such is the case for structures such as the flap track fairing, FTF. FTFs withhold the mechanisms of deployment of flaps. The one that motivated this study is aligned with an engine pylon. A method for simulating non-linear fluid structure interaction during transient response while minimizing the computational resources has been developed. The methodology uses a combination of structural and aerodynamic reduced order models, interpolation techniques and an efficient aero-structure data exchange. A test campaign has been expressly conceived to reproduce a similar but simpler mechanism of interaction to the one of the FTF and the jet to provide data for validating the

method of fluid structure interaction. In this paper the test set up and acquisition techniques are presented and the collected data and interpreted. A brief introduction to the validation of the methodology of fluid structure interaction through direct comparison between test data and simulation results will also be presented.

2 A BRIEF OVERVIEW OF THE FLUID STRUCTURE INTERACTION METHOD

The methodology used in this study has been developed as a tool to efficiently simulate fluid structure interaction when structural non-linearities in contact areas play a relevant role and the simulation time acts as a major constraint [1]. Structural deformations are hypothesized to be too small to generate a perturbation on the flow field, while no assumption is made on the intensity of displacements. This means that only rigid movements are allowed when updating the CFD model. To minimize the simulation time reduction techniques are applied on both the structural and aerodynamic models. The structural model is reduced via the Component Mode Synthesis technique, referred to as CMS. The aerodynamic model is reduced applying energetic considerations after Singular Value Decomposition, referred to as SVD [2]. More over aerodynamic CFD computations are run previous to the fluid structure interaction. A database of pressure on the component under analysis is created as a function of the active degrees of freedom of the component itself. Interpolation techniques are used to retrieve the pressure distribution at the real position of the component at each time step of the fluid structure interaction transient simulation. The fluid structure interaction scheme can be seen in the following figure 1.

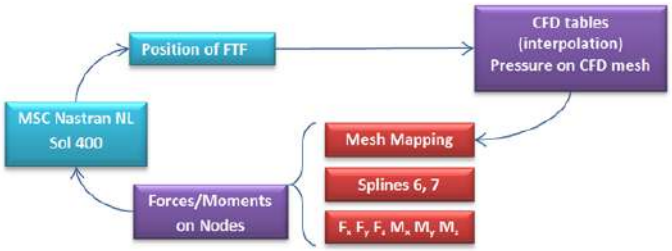

Figure 1: Simulation scheme for the FSI method

If a transient response simulation is launched, at $t = t_0$ the FE model is at a position (x_0, y_0, z_0) and it is loaded with the corresponding pressure distribution $\{F_k\}_0$. The aerodynamic pressures on the aerodynamic mesh $\{F_k\}$ are transposed onto the finite element mesh by multiplying the force vector for the matrix $[G_{kg}]^T$ [3], [4] built using the MSC HSA Toolkit™.

$$\{F_g\} = [G_{kg}]^T \{F_k\} \tag{1}$$

The structural solver moves forward of one step and the new position of the FE model at $t = t_1$ is calculated. The position is used to obtain the new aerodynamic load on the component $\{F_k\}_1$. The procedure continues as many times as specified.

3 TEST SETUP FOR DATA COLLECTION

The aim of the test campaign is to generate a sufficient amount of data to be used in the process of validating the aero-elastic toolbox developed for simulating fluid structure interaction problems. The test setup has been designed with the objective of distilling into a simplified system

the driving parameters of the complex interaction between a bulk body partially immersed in an asymmetrical fashion in an engine exhaust. The outputs of interest are the main frequencies of vibration of the bulk body under the aerodynamic excitation, the intensity of its displacement and the force levels observed at the attachments. The parameters that are identified as playing a major role on the outputs are the inertial, elastic and damping characteristics of the bulk body, its relative position with respect to the engine, the exhaust speed and the type of excitation. It is supposed that the aerodynamic excitation can be broken down as acting on two levels. The first level is at a low frequency when considering the resultant of the aerodynamic forces acting on the bulk body and pushing it away from its equilibrium position in opposition to the structural repealing force that will tend to bring back the bulk body to its equilibrium position. Secondly there are the vortices that originate from a Kelvin-Helmoltz instability due to the presence of a high speed flow and the surrounding still fluid. These turbulent structures impact on the bulk body and excite it at a higher frequency. This second source of excitation is not considered in this study that will focus on the global interaction between the bulk body and the engine itself.

3.1 Wind Tunnel

A subsonic, closed return wind tunnel is used for the test. The test vane is 70 centimeters long and has a squared transversal section of 45 by 45 centimeters.

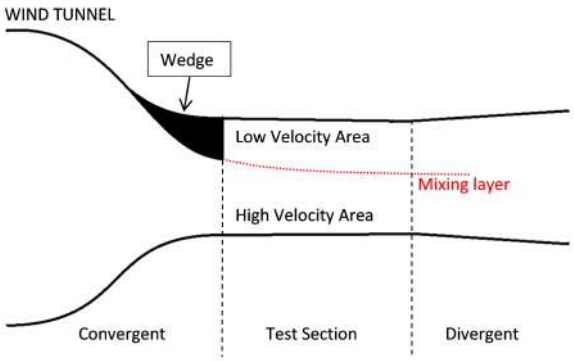

Figure 2: Wind Tunnel - view from above

The wind tunnel has been customized by adding a shaped wedge that partially obstructs the inlet of the test vane as shown in the following figure 2. This will create a speed gradient in the wind tunnel test section. More precisely there will be a high-speed and a quasi-zero speed area downstream of the wedge. A mixing layer will develop between the two zones. The maximum rotation engine speed is 2200 rounds per minutes, corresponding to an average speed of 35 meters per second in the high speed portion of the test section.

3.2 Mechanical Setup

The mechanical setup consists of a rectangular plate, mounted on a support that is in fact the wind tunnel test section. One of the two short edges of the plate is shaped in an arch form and it will be referred to as the leading edge since it faces the inlet of the wind tunnel. The other short edge is shaped as an isosceles triangle and it is referred to as the trailing edge. The plate is positioned on the support so that its leading edge is always immersed in the mixing layer, see figure 3.

The mechanical test setup can be seen in the following figure 4. The plate has just one degree of freedom. It is the rotation along the axis that passes through and is parallel to the leading

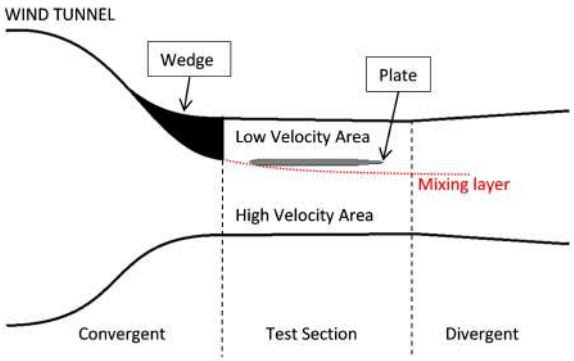

Figure 3: Test Set - View from above

edge. Another axis is press-fitted through the trailing edge. This axis is used to exert a repealing elastic force on the plate, when moved away from its equilibrium position, through the use of two springs in series on opposite sides of the axis. The equilibrium position of the plate is imposed by the position of the steel brackets where the other extremity of the spring is attached. One spring extremity is linked to the axis itself and the other to a bracket that can slide to allow the adjustment of the repealing force on the axis. This means that there are two brackets that are fixed symmetrically with respect to the trailing edge axis. By varying the angle of attack of the plate its trailing edge will be either plunging in the high speed portion of the wind tunnel test section or it will be completely out of it. The first configuration is referred to as negative angle of attack α, the second negative α. On each bracket an abutment is mounted in order to be able, if necessary, to limit the movement of the plate.

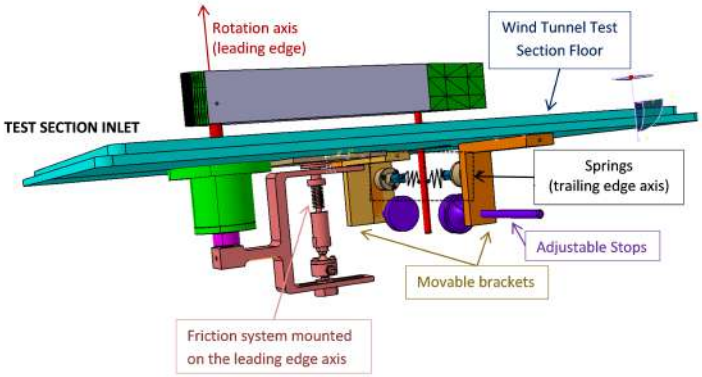

Figure 4: Test Set - Lateral view

A friction generating system is mounted on the leading edge axis. This system can be activated or deactivated. It consists of a fork that rotates integrally with the plate. On the fork a spring system exerts a pressure force onto a flat ring. This flat ring will therefore be in contact with the wind tunnel floor. When the plate rotates, the ring will follow the movement and it will generate a friction force by rubbing against the wind tunnel floor. This force causes a moment around the plate's axis that opposes its rotational motion. In a first phase of analysis four factors with three levels each have been identified influencing the output of interest. They are:

- Factor 1: Height of the plate
- Factor 2: Stiffness of the springs at the trailing edge
- Factor 3: Equilibrium position
- Factor 4: Wind Tunnel engine rotation speed

For each factor a low, medium and high level are defined, see table 1. The plate to be tested can be chosen between three available sizes to appreciate the influence of the inertial properties of the system. The springs mounted on the trailing edge axis will determine the elastic properties of the system and they can be chosen within three sets of different stiffness. The trailing edge of the plate is positioned in or out of the high speed portion of the test section, three values of angle of attack are chosen. The rotation speed of the wind tunnel engine determines the wind velocity in the test section, three levels are chosen.

Factor	Low	Medium	High
Height [m]	0.05	0.10	0.15
Stiffness [N/m]	170	300	910
Equilibrium position [°]	-3	0	3
Wind Speed [m/s]	23.76	27.72	32

Table 1: Levels of the factors

3.3 Design of experiment

The core of the test experience consists in the observation and acquisition of the desired outputs. Before starting with it, it is important to lay down a plan depicting the parameters that influence the system and their combination during each test run. This procedure is called *design of experiment*. The test set has been conceived with several tunable parameters that can influence the observed behavior of the test set itself. These adjustable parameters will be referred to as factors. Each factor can assume a certain number of values, these are called levels. The combination of factors and level during each test run is indicated by the L9 Taguchi [5] fractional factorial table, see table 2.

N°test	Level			
	A	B	C	D
1	1	1	1	1
2	1	2	2	2
3	1	3	3	3
4	2	1	2	3
5	2	2	3	1
6	2	3	1	2
7	3	1	3	2
8	3	2	1	3
9	3	3	2	1

Table 2: L9 Taguchi Table

Each test run is repeated three times to have an information on the scattering and check the repeatability of the experiments. The testing activities are mainly divided in three parts. First, acquisitions with the technique of Particle Image Velocimetry, PIV, are carried out. Once the characteristics of the flow in the wind tunnel are known, a vibration assessment is carried out. It consists of a hammer testing of the non-operating wind tunnel with the mechanical test setup. This is finally followed by stress and acceleration acquisitions simultaneous to displacement measurements with laser displacement sensors of the mechanical test setup while the wind tunnel is operating at the desired speed.

3.4 Instrumentation

3.4.1 Particle Image Velocimetry

Particle Image Velocimetry [6] is a non-intrusive flow measuring technique that consists in recording the displacement of small particles embedded in a region of fluid to reconstruct the velocity field in the laser plane. The dual laser head system Gemini ™PIV 200-15 is used for the test and has the following characteristics:

- Emission wave length: 532.0 nm
- Nominal frequency: 15 Hz
- Maximum energy per pulse: 2x200 mJ
- Diameter of the laser beam: 5mm, divergence <2
- Nominal pulse duration: 3-5 ns

The laser is mounted on a beam that in turn is fixed on a tripod. Its vertical position is remotely controlled via a computerized system. This will enable to displace the laser head and to light the wind tunnel section at different stations with the intention of verifying the vertical continuity of the flow. The camera is also mounted on a beam situated on top of the wind tunnel test section, see figure 5.

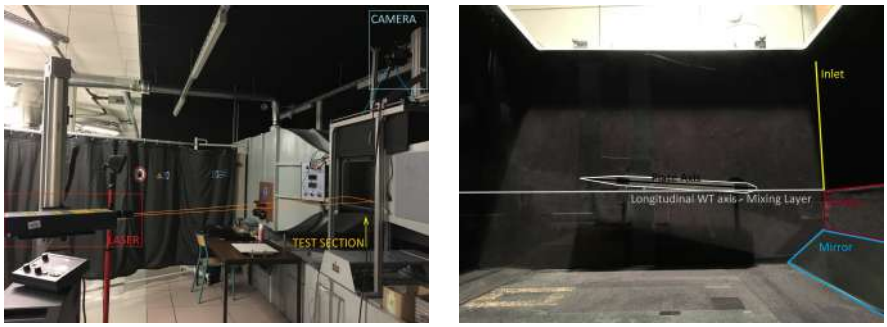

(a) Lateral view (b) View from above

Figure 5: View on the test installation

3.4.2 Tap Test

Some preliminary testing is carried out to identify the behaviour of the mechanical setup and its possible interactions with the wind tunnel where it is installed [7]. A tap test is a technique of experimental modal analysis that allows to determine the natural characteristics of a structure which are the frequencies, damping and mode shapes. The *roving hammer* is the technique of choice for testing the wind tunnel and the mechanical set, which consists in putting the accelerometers in some fixed positions on the structure and then impacting it at several locations. Two tap tests are carried out, one on the wind tunnel with the mechanical test and another one on the plate and its axis clamped on a test bench.

The material used for the analysis of the system wind tunnel, mechanical set is hereby described and can be seen in figures 6(a), 6(b), 6(c):

- Five mono-axial accelerometers:
  - one is placed on the floor of the wind tunnel test section, in z direction;
  - two are placed in the wind tunnel test section frame, one in y and one in -x direction;

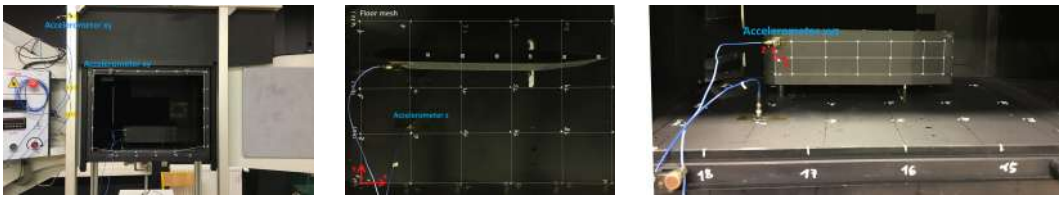

(a) WT frame mesh (b) WT floor mesh (c) Plate mesh

Figure 6: Wind tunnel tap test setup

  - two are placed in the *Norcan* frame wrapping the wind tunnel, one in y and one in x direction.
- One tri-axial accelerometer, placed on the plate.
- One hammer for impact with a hard and a soft plastic tip.

For the tap test of the plate on the bench, a single tri-axial accelerometer is put on the plate, see figure 7.

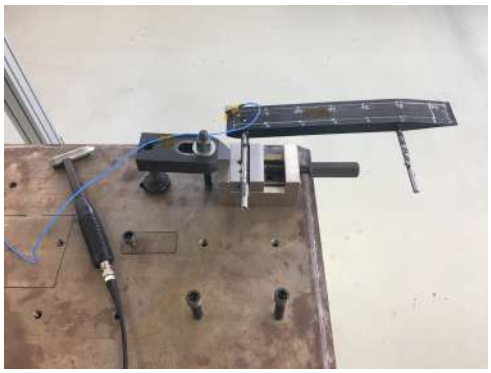

Figure 7: Bench tap test setup

3.4.3 Force, acceleration and displacement acquisition

The main objective of the test campaign is to monitor the behaviour of the plate and of the system where it is mounted on when they are immersed in a fluid flow with a neat discontinuity in speed. In order to do so sensors are positioned in several locations of the test installation. The acceleration of the plate is measured in a single point. The plate is in fact sufficiently thick to behave rigidly throughout the test. The accelerometer is positioned on the trailing edge axis, see figure 8(a).

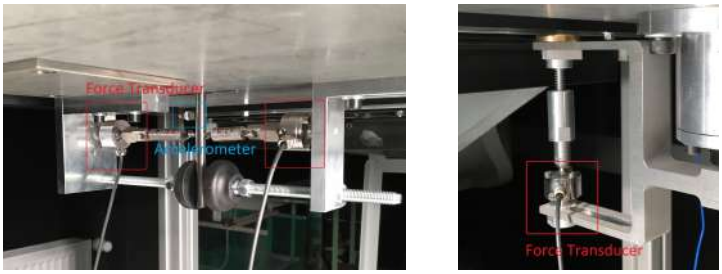

(a) Trailing Edge (b) Leading Edge

Figure 8: Axis acquisition systems

In parallel with the springs linked to the trailing edge axis there are two force sensors. Their frequency of acquisition is 0.2 MHz. In parallel with the spring in the fork-system at the leading edge axis a third force sensor is mounted. Its frequency of acquisition is again 0.2 MHz. This sensor measures the force exerted on the ring that rubs on the wind tunnel floor for friction. Two laser displacement sensors are used to measure both the displacement at the trailing edge of the plate and of the wind tunnel frame in the same plane. They are placed on a table in front of the glass wall of the wind tunnel test section as shown in figure 9 *(a)*. The table is positioned at a certain distance from the wind tunnel so that it is not subjected to vibrations induced from the wind tunnel itself.

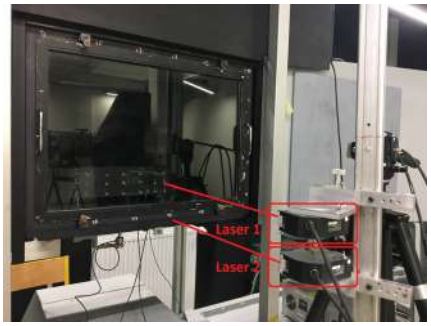

Figure 9: Laser displacement sensors

The laser measures positive and negative displacements around a position of reference that is the zero. As a default the zero is at 300 mm of distance from the laser head. Measurements can be done up to 500 mm from the zero and -250 mm. It is possible to control the measurement area, by adjusting the interval 0-10 V to the length-span of interest around the zero. The zero can also be displaced of a certain offset always within the measurement range of the laser. In this case the zero is set on the plate trailing edge when α is equal to zero. The laser has a sampling frequency of 50 kHz. With the above mentioned laser only the component along the transverse axis of the wind tunnel of the displacement can be measured. The recording of all the outputs listed above is done simultaneously by using the HBM™GENESIS acquisition system. The system is equipped with six channels. A trigger mode is available and it is programmed to set off the acquisition when the force level sensed at the trailing edge springs exceeds a certain threshold. The sampling frequency is set at 2.5 kHz for all the signals. Each acquisition is triggered simultaneously when the level of force at the sensors in the trailing edge of the plate reaches 0.8 N. Each acquisition lasts 20 seconds.

4 MODELS OF THE TEST SETUP

4.1 CFD Model of the Wind Tunnel

The computational fluid dynamic mesh is composed by two separate unities, the wind tunnel, see figure 10(b), and the plate, see figure 10(c), later assembled through over-set grid approach, see figure 10(a).

Two methods of computational fluid dynamics for fluid simulation are used to recreate the fluid flow in the wind tunnel and their results are compared. The two methods are time-averaged Unsteady Reynolds Averaged Navier Stokes, URANS, and a Lattice Boltzmann method, LBM.

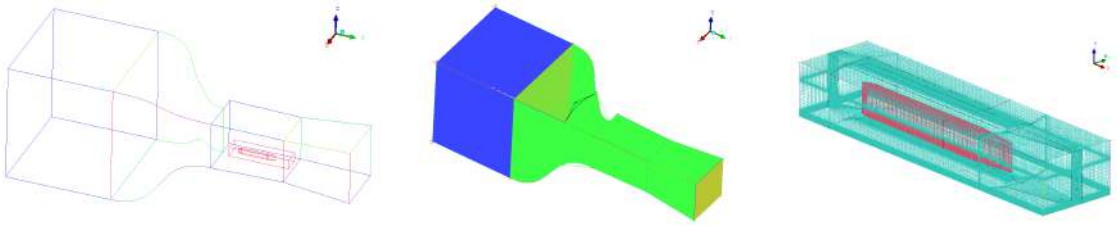

(a) Geometry wind tunnel and plate mesh (b) Wind Tunnel mesh (c) Plate mesh

Figure 10: Wind tunnel tap test setup

4.1.1 Averaged URANS

In the Unsteady Reynolds averages Navier stokes method each istantaneous quantity is decomposed into a time averaged part, a resolved fluctuation and the modelled turbulent fluctuation. The *Spalart-Allmaras* is turbulence model of choice. The results of the unsteady computation are averaged over time a posteriori. The solver used for this type of simulations is elsA™ [8] and the characteristics of the flow are listed in table 3.

Flow property	Value
Reynolds N°test vane[-]	723333
Temperature [K]	288.15
Mach N°test vane [-]	0.09

Table 3: URANS parameters

The Reynolds number is calculated with respect to the chord of the plate. The mesh of the wind tunnel is composed by 15409152 elements and the mesh of the plate by 1916928. The plate has been discretized span-wise with 33 points, chord-wise with 99. The dimension of the first cell layer at the plate skin is 11 µm to obtain an y^+ of 1 for a flow speed of 31 m/s.

4.1.2 LBM

A Lattice-Boltzmann Method, referred to as LBM, is used to perform a Large-Eddy Simulation of the flow in the wind tunnel configuration. The LBM considers the discrete Boltzmann equation, a statistical equation for the kinetics of gas molecules. Thus, the primitive variables of the LBM represent the statistical particle probability distribution function, to which the usual macroscopic variables pressure and velocity relate as velocity moments. Beyond its computational performance, the main advantage of LBM is that the method is stable without artificial dissipation, which makes it equivalent to solve the Navier-Stokes equations with a high-order numerical scheme [9]. The present discretization of the equations ensures the method is second order accurate both in time and space. The LBM equations are solved using the open source software Palabos (www.Palabos.org), developed by the University of Geneva. The mesh of the wind tunnel and plate is composed by 459143376 elements. The plate has been discretized span-wise with 62 points, chord-wise with 473. The dimension of the first cell layer at the plate skin is 667 µm to obtain an y^+ of 60 for a flow speed of 31 m/s, following the law of the wall.

4.2 Finite Element Model of the Mechanical setup

The finite element model of the mechanical setup is made using the MSC Nastran™*Sol 400* FE solver and it is composed by a simple plate, lying on the x-z plane, and the two axis, one at the

leading edge of the plate and one at the trailing edge of the plate.

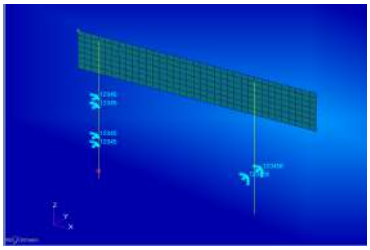

Figure 11: Finite Element Model

The axis at the leading edge is constrained in five degrees of freedom in correspondence to the bearings of the real system, leaving the plate free to rotate only around the z axis. A mass is also attached to the leading edge axis with an inertia equal to the one of the real friction-fork system. The trailing edge axis is attached to two spring elements (CBUSH are used). The springs are aligned with the y axis and are positioned at opposite sides of the axis. One of the extremities of the spring is attached to the axis, the other is clamped on the 6 DoF. The attachment between plate and its axis is hypothesized to be perfect. The model can be seen in figure 11.

5 VALIDATION

This section will show the comparison between test data and numerical simulation of the test setup. First the mechanical setup and the wind tunnel will be analyzed separately. Then the data collected during fluid structure interaction testing will be analyzed.

5.1 Particle Image Velocimetry

The wind tunnel has been customized for the test, therefore it has been necessary to run some test aimed at characterizing the fluid flow field in the test vane. The outcome of these tests is here compared to the CFD simulations of the wind tunnel in the same configuration.

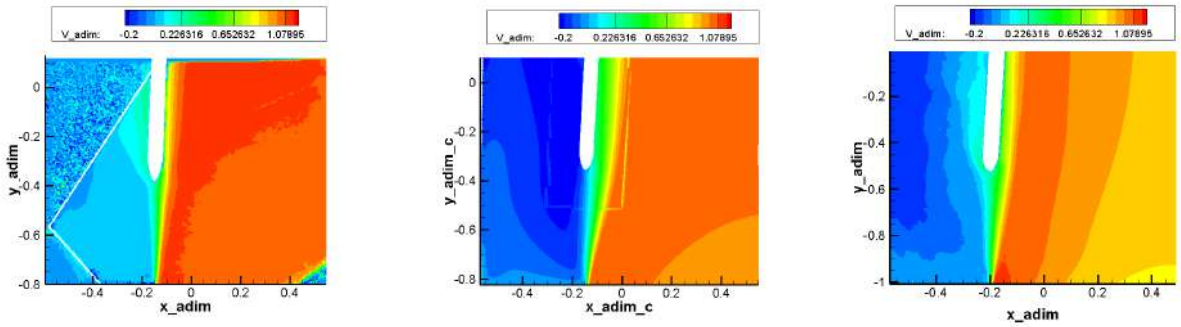

(a) PIV (b) Averaged URANS (c) LBM

Figure 12: Comparison PIV, averaged URANS and LBM

In figure 12 the test and simulation averaged flow velocity field can be seen in (a) and (b) respectively. With the PIV test it is not possible to visualize the whole flow field by using a single laser because the plate is not transparent. To extend the vision field, a mirror at 45° has been added in the left corner of the test section, in correspondence to the wedge. In figure 13 the streamlines are drawn. The major differences between test and simulations occur in the low speed zone of the wind tunnel and in the mixing layer. In particular the PIV test shows the

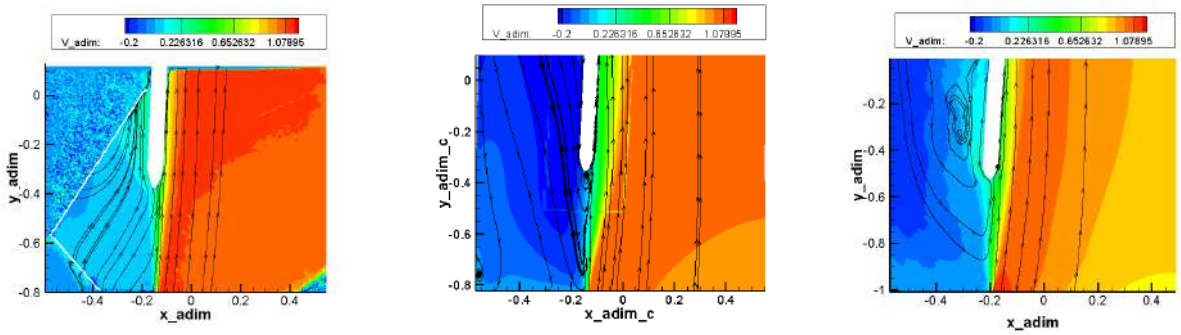

(a) PIV (b) Averaged URANS (c) LBM

Figure 13: Comparison PIV and averaged URANS - streamlines

presence of a re-circulation bubble on the left side of the plate pretty closed to the leading edge. This bubble in the averaged URANS computations is found closer to the trailing edge of the plate while in the LBM computations two re-circulation bubbles are present: one next to the leading edge and one next to the trailing edge. It is concluded that this phenomena does not have a big influence on the pressure distribution computation since in that zone the airspeed is close to 0 m/s. On the other hand, simulations give a thicker mixing layer and with a higher curvature.

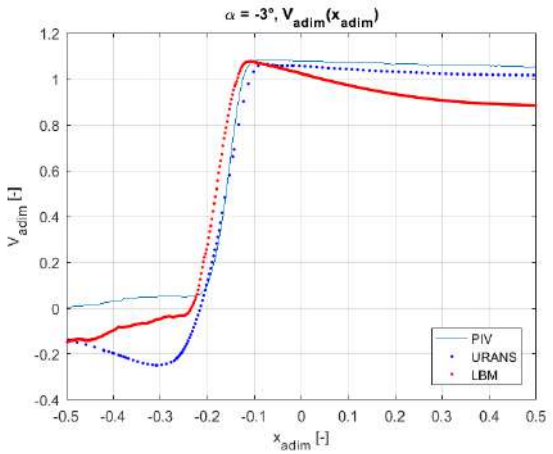

Figure 14: Speed at y = -0.45

In figure 14 the non-dimensional speed is drawn in function of the non-dimensional x coordinate for test and simulations. It is possible to see that simulations give negative speeds on the left side of the plate and a thicker mixing layer. Overall the simulations give a satisfying representation of the wind tunnel flow field.

5.2 Tap Test

A first tap test is carried out on the full testing system composed by wind tunnel and mechanical test with the objective of identifying possible interactions between the components. Lightly damped modes appear at very low frequency. The list of those that are relevant for the study is reported in table 4, in the second column the frequency is reported in *Hz* while in the third column the damping coefficient associated with the mode can be seen.

The first mode at 5.87 Hz is an asymmetric bending of the wind tunnel frame, the displacement

Mode N° [-]	f [Hz]	ζ[%]
1	5.87	1.33
2	7.90	0.74
3	15.15	1.99
4	23.63	9.68
5	26.17	3.64
6	30.72	13.23
7	35.02	0.85
8	39.86	6.54
9	44.59	6.00

Table 4: Modes of the whole test set

is maximum in the higher right corner in correspondence to the inlet of the wind tunnel test section. The asymmetry is accentuated by the presence of the wedge and the mirror. Floor and ceiling of the test section seem to be also attached to the wind tunnel body in a different way: the floor is bolted while the ceiling is not. The second and third mode see the activation of the lateral displacement also in the left frame. To be noted that the movement of the frame is transmitted to the plate that responds with a tri-dimensional movement. The appearance of the fourth and fifth mode is caused by the boundary conditions at the attachment of the plate and the wind tunnel floor. The sixth mode is a bending of the wind tunnel. Torsion of the wind tunnel appears at 44 Hz. Discovering these modes has influenced the choice of acquisition techniques for the fluid structure interaction tests.

A second tap test is carried out on the plate clamped on a test bench. The FE model of the plate is optimized and validated with the results of this last tap test. The optimization procedure is done through a MSC Nastran™ *Sol200* to make sure that the computational low frequency modes of the plate match the ones identified during the tap-test for the plate in the same configuration. The FE modes under 100 Hz are matched to the ones identified in the same frequency bandwidth through tap testing. The optimization variables are the plate thickness and the diameter of the two axis. The function to be minimized is the following:

$$\begin{aligned} f(f_{1_{test}}, f_{2_{test}}, f_{3_{test}}, f_{1_{fem}}, f_{2_{fem}}, f_{3_{fem}}) = \\ = \sqrt{(f_{1_{fem}} - f_{1_{test}})^2 + (f_{2_{fem}} - f_{2_{test}})^2 + (f_{3_{fem}} - f_{3_{test}})^2} \end{aligned} \tag{2}$$

The error accepted over the FEM frequencies is of 5%.

5.3 Wind Tunnel Testing

The mechanical system is composed by the plate and its support and it is placed in the wind tunnel test section. Each run of the test consist in a calibration of the parameters and an acquisition over the channels with the active wind tunnel. The sensors are calibrated before starting the wind tunnel by equilibrating to zero the *Wheatstone* bridge. Afterwards the engine of the wind tunnel is started and the power is adjusted. The acquisition is triggered when the level of force in the sensors at the trailing edge of the plate is superior than 0.8N. The time signals are acquired through the *GEN* system for 20 consecutive seconds and data is transferred on hardware through the *Perception*™software in ASCII format. The signals are then re-loaded

and post-processed using *Matlab*™. Signals are under-sampled, filtered, and converted into frequency domain data through Fourier transform. Several visualization methods are then applied to extract information and interpret them.

5.4 Analysis of parameter interaction during the FSI testing

The main effect graph show how different levels of a factor affect the response by plotting the response mean for each factor level connected by a line. In the following figure 15 the influence of the factors on the first frequency of vibration can be seen. In figure 16 the maximum delta displacement of a point at the trailing edge of the plate is plotted versus the four factors.

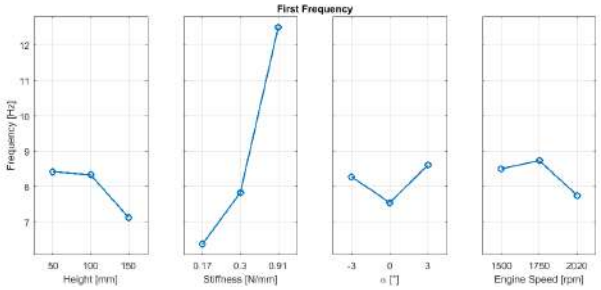

Figure 15: Main Effect Plot - First Frequency

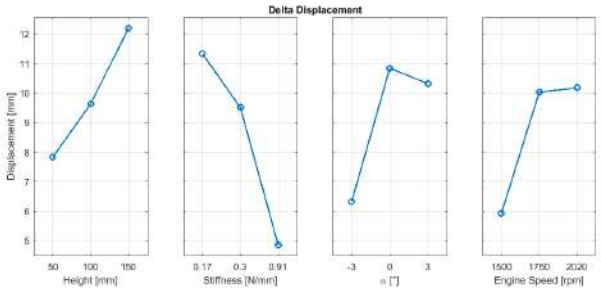

Figure 16: Main Effect Plot - Displacement

It can be seen that the factors that have a stronger influence on the first frequency of vibration are the stiffness of the system and the height, therefore the mass, of the plate. The stiffness in particular is the most relevant factor and it can be seen that the higher the stiffness, the higher the first frequency will be. It can also be noticed that the interactions between frequency and factors are non linear. The maximum displacement of the plate is influenced by all the four factors, but the driving parameters are the stiffness and the position of equilibrium. In particular the higher the stiffness, the lower the displacement will be. Displacement as a function of position of equilibrium and displacement as a function of the engine speed are non linear relations.

A more in depth analysis is done by plotting one of the outputs as a function of one factor for several values of another factor. For example in figure 17 *(a)* the first frequency of vibration is a function of the equilibrium position α, and the various curves refer to several values of the stiffness at the trailing edge of the plate, k. In figure 17 *(b)* the maximum and mean displacement are a function of the equilibrium position for several values of the stiffness k. The maximum displacement is the maximum amplitude of displacement recorded during the test. The mean displacement corresponds to the position around which oscillations take place during a single test. If α is fixed at a certain level, frequency is higher if the stiffness is higher. But if the stiffness is fixed it is possible to see how the frequency doesn't change that much. The maximum

amplitude of displacement measured, as previously stated, is higher for higher alpha. The position of equilibrium changes inversely proportionally with alpha, and with the position of the movable brackets.

(a) (b)

Figure 17: Influence of α on the first frequency and on displacement

In figure 18 frequency is a function of the plate height, in *(a)*, and the maximum and mean displacement are a function of the plate height, in *(b)*. On the same graph, curves associated to different value of stiffness are drawn.

(a) (b)

Figure 18: Influence of the plate height on the first frequency and on displacement

If the height is fixed at a certain value frequency increases with stiffness. The behavior of the maximum displacement amplitude is a slightly more complex. For high stiffness displacement increases with the height of the plate. For low stiffness the behavior is no longer linear, when the inertia term is too high for the stiffness the displacement diminishes.

(a) (b)

Figure 19: Influence of stiffness on the first frequency and on displacement

In figure 19 frequency is a function of the stiffness, in *(a)*, and the maximum displacement is a function of the stiffness, in *(b)*. On the same graph, curves associated to different value of equilibrium position are drawn. If the stiffness is fixed at a certain value it is possible to see how for negative or null angles there is no influence on the frequency, whereas frequency changes for positive values of α. The behavior of the maximum amplitude of displacement is straightforward. The higher the stiffness the lower the displacement for every equilibrium position.

In a second stage of the testing activities friction is added to the list of parameters, while the equilibrium position and the speed are no longer considered. Hence the parameters are three: height of the plate, stiffness of the springs at the trailing edge of the plate and friction. The procedure followed to analyze the time signals and interpret the results is slightly different. Under-sampling and filtering are still carried out. A direct comparison between condition with and without friction is preferred to the main effect plot. The plate considered fr the first comparison measures 100 mm in height, the stiffness of the springs in the trailing edge is 0.08 N/mm, the equilibrium position is set at an angle of 0° with respect to the longitudinal axis of the wind tunnel, the rotation speed of the engine is 2020 rpm, and when friction is added Teflon is chosen.

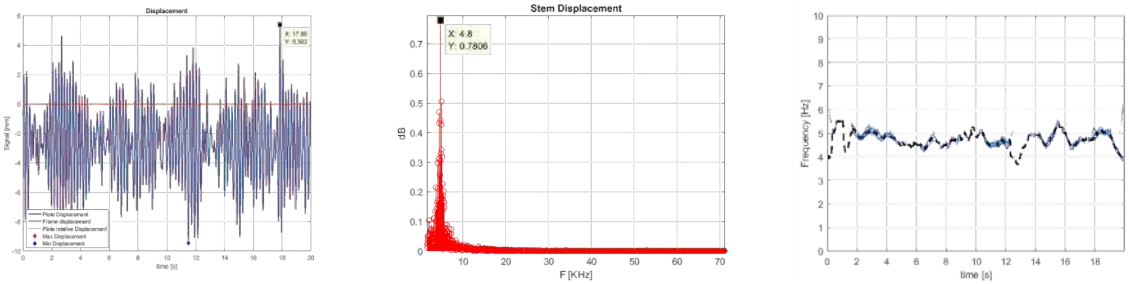

(a) (b) (c)

Figure 20: Displacement Signal H_{plate} = 100 mm, k = 0.08 N/mm

Figure 20 shows in *(a)* the displacement time signal recorded at the trailing edge, in blue, and the one recorded in the frame of the wind tunnel, in copper. The maximum amplitude recorded is of 13 mm. In *(b)* the stem plot of the Fast Fourier Transform shows a very clean peak at 4.8 Hz. In *(c)* the time-frequency ridges from wavelet synchro-squeezing plot can be seen. The maximum energy time-frequency ridge is extracted in cycles per sample of the wavelet synchro-squeezed transform. Each ridge is a separate mode of the signal. In this case the evolution through time of the frequency of the first mode is followed and it can be seen that the signal does not change very much over time. An oscillation around the fundamental value of 4.8 Hz can be observed.

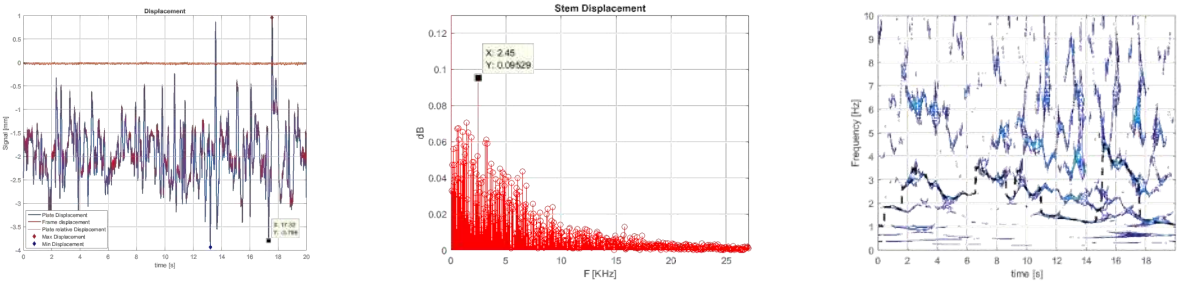

(a) (b) (c)

Figure 21: Displacement Signal H_{plate} = 100 mm, k = 0.08 N/mm, Teflon/Steel

Adding a dissipative element in the system changes drastically its answer. Figure 21 shows

how the time signal is more noisy, see *(a)*, and it is difficult to identify a single peak after transforming the signal into the frequency domain. The energetic content is distributed over a larger frequency-bandwidth. If the evolution through time of peak at 2.45 Hz is followed, it can be seen that there is no longer an oscillation around a defined frequency, but the curve shows sudden jumps as if the nature of the behavior of the system was changing from a mode to another. This means that the recorded signals are of short duration, and change substantially over time.

6 CONCLUSIONS AND PERSPECTIVES

This paper describes the test setup and data collection techniques for validating through direct comparison a method for fluid structure interaction. A closed-return wind tunnel as been customized to create a flow discontinuity in the test vane. A mechanical setup composed by a plate, two axis a friction system and a repealing elastic system has been built in the wind tunnel test section floor. The mechanical behavior of this test set-up has been studied through impact testing. The flow in the wind tunnel test section has been characterized through particle image velocimetry. The interaction between the mechanical setup and the aerodynamic field in which it was immersed has been monitored through the use of displacement, acceleration and force sensors. The FE model of the mechanical setup has been tuned using tap test results. The boundary conditions of the CFD computations have been adapted in order to obtain the desired coherence between simulations and particle image velocimetry data. The fluid structure interaction data have been analyzed to identify the interactions between the design parameters and their influence on the observed outputs. In particular the stiffness and mass properties of the system are the parameters that drive the first frequency of vibration of the system. The amplitude of the oscillations is sensitive to all factors variation: flow-speed, equilibrium position, stiffness and mass. The data collected during the test campaign are currently being exploited to complete the validation of a fluid structure interaction method developed to answer the complex industrial problem of efficiently simulating fluid structure interaction when structural non-linearities at contact play a relevant role and the simulation time acts as a major constraint.

7 REFERENCES

[1] Bosco, E., Lucchetti, A., Trapier, S., et al. (2016). Nonlinear transient fluid/structure interaction approach using surrogate models: Industrial application to aircraft fairing vibration excited by engine efflux. In *15th Dynamics Specialists Conference*. p. 2049.

[2] Sadek, R. A. (2012). Svd based image processing applications: state of the art, contributions and research challenges. *arXiv preprint arXiv:1211.7102*.

[3] Charbel, F., Lesoinne, M., and Le Tallec, P. (1998). Load and motion transfer algorithms for fluid/structure interaction problems with non-matching discrete interfaces: Momentum and energy conservation, optimal discretization and application to aeroelasticity. *Computer methods in applied mechanics and engineering*, 157(1-2), 95–114.

[4] Di Vincenzo, F. G., Kwiatkowska, M. V., Leonteva, R. V., et al. (2015). Analysis of flight loads and static aeroelasticity characteristics of the airplane with the use of three-dimensional aerodynamics. *International Forum of Aeroelasticity and Structural Dynamics Proceedings*.

[5] Nair, V. N., Abraham, B., MacKay, J., et al. (1992). Taguchi's parameter design: a panel discussion. *Technometrics*, 34(2), 127–161.

[6] Adrian, R. J. (2005). Twenty years of particle image velocimetry. *Experiments in fluids*, 39(2), 159–169.

[7] Ewins, D. J. (1984). *Modal testing: theory and practice*, vol. 15. Research studies press Letchworth.

[8] Cambier, L. and Veuillot, J. (2008). Status of the elsa cfd software for flow simulation and multidisciplinary applications 46th aiaa aerospace science meeting and exhibit (reno, usa).

[9] Marie, R. D., S. and Sagaut, P. (2009). Comparison between Lattice Boltzmann method and Navier-Stokes high order schemes for computational aeroacoustics. *Journal of Computational Physics*, 228(4), 1056–1070.

COPYRIGHT STATEMENT